



Bin Mohd Rashid, M. S. R., Zheng, J., Sng, E., Rajendhiran, K. M., Ye, Z. and Lim, L. H. I. (2021) An enhanced cloud segmentation algorithm for accurate irradiance forecasting. *Solar Energy*, 221, pp. 218-231.  
(doi: [10.1016/j.solener.2021.03.061](https://doi.org/10.1016/j.solener.2021.03.061))

There may be differences between this version and the published version.  
You are advised to consult the published version if you wish to cite from it.

<http://eprints.gla.ac.uk/239973/>

Deposited on 26 April 2021

Enlighten – Research publications by members of the University of Glasgow  
<http://eprints.gla.ac.uk>

# An Enhanced Cloud Segmentation Algorithm for Accurate Irradiance Forecasting

Muhammad Syazwan Rifdi Bin Mohd Rashid<sup>a</sup>, Jinghong Zheng<sup>b</sup>, Ernest Sng<sup>c</sup>,  
Kurinji Malar Rajendhiran<sup>d</sup>, Zhen Ye<sup>e</sup>, Li Hong Idris Lim<sup>a,\*</sup>

<sup>a</sup>University of Glasgow, Glasgow G12 8QQ, UK

<sup>b</sup>Institute for Infocomm Research, A\*STAR, 1 Fusionopolis Way, #21-01 Connexis,  
Singapore 138632

<sup>c</sup>REC Solar Pte Ltd, 20 Tuas South Avenue 14, Singapore 637312

<sup>d</sup>Ngee Ann Polytechnic, 535 Clementi Rd, Singapore 599489

<sup>e</sup>Leica Microsystems, 12 Teban Gardens Cres, Singapore 608924

---

## Abstract

This paper presents a novel approach to calculate cloud cover under any illumination conditions for short-term irradiance forecasting. A sky-imaging system, in parallel with an irradiance measurement, is set up to collect a database of sky images and irradiance readings. The colour space operations and various image segmentation methods are investigated to improve the visual contrast of the cloud component. Experimental results shows the effectiveness of applying the Normalized Blue-to-Red Ratio (NBRR) colour operation for high-illumination condition and the Red/Green channel for the low-illumination condition. The pre-processed sky images are then fed into Minimum Cross Entropy (MCE) adaptive thresholding segmentation, which effectively differentiates the sky and cloud components for all-sky images. The cloud fraction calculation is employed for the segmented images as an indication of cloud coverage. The proposed method demonstrates a positive linear correlation between cloud fraction and real-time irradiance data.

*Keywords:* Sky-Cloud Segmentation, Solar Irradiance Forecasting, Cloud Fraction

---

## 1. Introduction

The minuscule size of Singapore gets the city-state ranked 16th and 24th out of 143 countries in the highest main energy consumption and carbon emission per capita, respectively [1]. To address this grievous issue, Singapore intends to reduce its emission intensities by promoting solar power as a renewable source of energy. In 2016, in efforts to meet the nation's goal, Housing & Development

---

\*Corresponding author

Email address: [lihonidris.lim@glasgow.ac.uk](mailto:lihonidris.lim@glasgow.ac.uk) (Li Hong Idris Lim)

Board (HDB) and Economic Development Board (EDB) initiated the SolarNova programme that aims to boost solar adoption power to 350MWp by 2020 [2]. This rising demand for power production from photovoltaic (PV) systems im-  
10 mensely intensifies the need for accurate solar irradiance forecasting.

However, to obtain accurate forecasting of irradiance, cloud information must be integrated into the formulation as volatility in solar irradiance is largely caused by cloud motion [3]. Solar PV generation farms contingent upon cloud cover information as cloud cover modulates the solar radiation incident on the  
15 solar panel’s surface [4]. As a result, grids that rely heavily on solar harnessing will experience major system fluctuations, thus significantly reducing the PV energy yield [5].

Ground-based sky imaging devices are commonly utilized to provide a hemi-spherical outlook of the sky, thereby allowing cloud cover to be measured [5].  
20 A precondition to distinct sky and cloud components in the captured sky-cloud image is segmentation, but there remain challenging complexities due to ambiguous cloud structures and a wide range of sky illumination condition. Although various existing cloud segmentation methods are thorough [6, 7, 8, 9], these methods primarily focus on cloud detection under a clear day high-illumination  
25 condition.

Irradiance does not only occur under high-illumination condition but 24-hours a day, where the sky luminance distribution is solely due to the position and travel path of the sun. In light of the approaches in the literature, to the best of our knowledge, there has not been an investigation analysis regarding  
30 on cloud segmentation under low-illumination conditions.

This paper aims to mitigate such a gap with an empirical image processing for accurate cloud cover detection under low-illumination condition. The proposed algorithm allows for a robust cloud segmentation framework to determine cloud cover under any illumination conditions. This enables better solar  
35 variability management for PV power stations so that pre-emptive actions can be taken for variable power generation from alternative sources in forecasted low-irradiance times.

## 2. System Setup

### 2.1. Sky Camera Setup

40 Acquisition of the locally captured images is obtained from the ground-based camera, located at Solar Park, Block 39, Ngee Ann Polytechnic, Singapore ( $1^{\circ}19'59.8''$  N,  $103^{\circ}46'21.8''$  E). The core component is a NIKON D7000 Digital Single Lens Reflex (DSLR) camera, with a 16 megapixels RGB CMOS sensor. The camera is equipped with an AF-S DX NIKKOR 18-200mm f/3.5-5.6G ED  
45 VR II lens, which provides a viewing angle of  $76^{\circ}$ . The camera is mounted on a tripod stand, adjacent to the solar PV panel and the irradiance sensor. This sky imaging setup demonstrates the added advantage of a simple, yet robust and small form factor built, as shown in Figure 1 (a).

The camera is set to shoot images manually with the settings – aperture of  
50 f/25, exposure time of 1/2500s, ISO of 6400 and focal length of 31mm. The

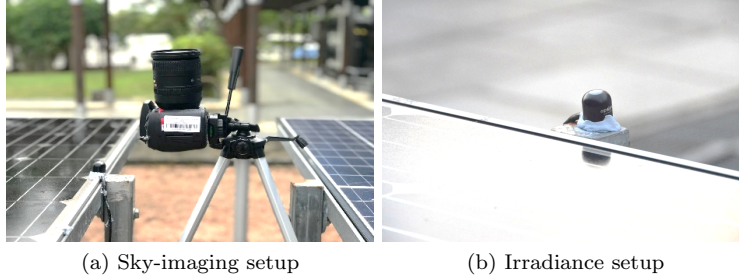


Figure 1: Measurement setup

images are captured with a resolution of  $4928 \times 3264$  pixels and stored as RGB colour format JPG images. To reduce the computational costs, the square area of the acquired image is considered and cropped, then resized to  $200 \times 200$  pixels.

### 2.2. Irradiance Sensor Setup

55 A solar irradiance sensor named Smart Pyranometer SP-420 by Apogee Instruments, is utilised to capture the Global Horizontal Irradiance (GHI) data. The cost-effective silicon-cell pyranometer has a field view of  $180^\circ$  and demonstrates a fast response time of less than 1ms. No datalogger is required as the sensor can be connected to a laptop via a USB 2.0 type A plug directly. The  
 60 ApogeeConnect software gives the user control of data logging settings while also providing real-time output display and graph measurements. The irradiance readings were collected at 1-minute interval consecutively. The pyranometer setup is depicted in Figure 1 (b).

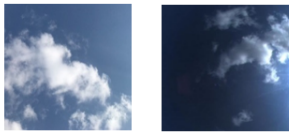
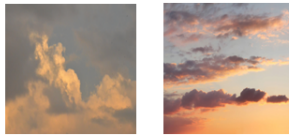
### 2.3. Classification of Sky-Cloud Images

65 Sky-cloud images under varying illumination conditions impose varying characteristics to distinguish clouds and sky component. From the perspective of image analysis, the histogram yields differing distribution in the RGB spectra. Therefore, to analyse and inspect the sky-cloud images under each illumination condition, there exists a need to provide a classification for the sky-cloud im-  
 70 ages. The proposed classification is to break down the sky-cloud images into two categories: low-illumination and high-illumination. The proposed classification is depicted in Table 1.

## 3. Colour Space Evaluation

As clouds possess indefinite and erratic features, most works use RGB colour  
 75 model as the primary characteristic for distinguishing cloud from the sky [6, 7, 9, 10]. Hence, to fully take advantage of colour information given in a sky-cloud image, the utilization of colour spaces is essential as it presents useful colour information for cloud detection analysis.

Table 1: Proposed classification of sky-cloud images

Category	Sky-Cloud Images	Irradiance Value
High-Illumination		$> 100 \text{ W/m}^2$
Low-Illumination		$< 100 \text{ W/m}^2$

### 3.1. Colour Space Operation for High-Illumination Sky Images

80 Numerous literatures have employed the colour operations of red and blue channels for cloud segmentation under high-illumination conditions or blue and white sky-cloud images [6, 7, 9]. To assess the colour channel operation suitable for the high-illumination condition, the histogram of the original RGB image is firstly extracted to depict the image statistical information visually. The histogram graph shows the count of pixels at each different pixel intensity found in the image. 85 The histogram graph shows the count of pixels at each different pixel intensity found in the image. Figure 2 shows the distribution of pixels amongst the grayscale values of an 8-bit channel image in the 256 different possible intensities.

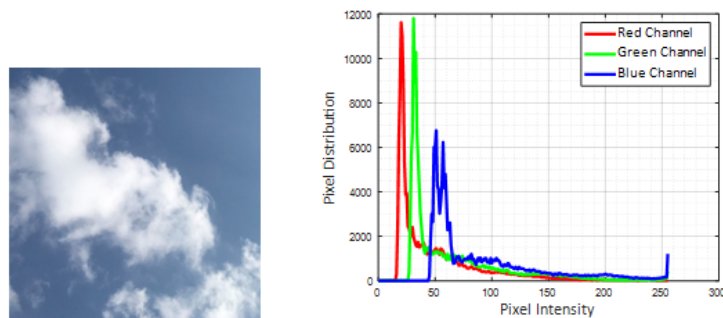


Figure 2: Origin and histogram of Image A

Visually inspecting into the histogram of Image A, the red spectrum can be seen closer to the lower end of pixel intensity (0), resulting in a darker image. In contrast, the Blue (B) channel has more useful information. With its spectrum distributed at the higher intensity portion, it yields a brighter image. With the colour information resulting at two ends, the scattering difference between these two channels results in the distinction of clouds. To further improve the visual contrast of the clouds against the sky, the R-B value was then normalized over the addition of both channels. This colour channel operation was also reviewed 95

in the literature in [6]. The normalized blue/red ratio, NBRR, is given by

$$NBRR = \frac{Blue - Red}{Blue + Red}. \quad (1)$$

Image B in Figure 3 shows the example of uneven brightness distribution across the sky-cloud image. Similar to the analysis of Image A, the red spectrum shows little information which results in a dark image, as shown in Table 2. On the other hand, Blue channel shows the most information and yields in a brighter image, as compared to the red channel. The NBRR operation of this image here improves the visual distinction of the clouds from the sky. In conclusion, the High-Illumination category can be well treated with the NBRR colour operation channel.

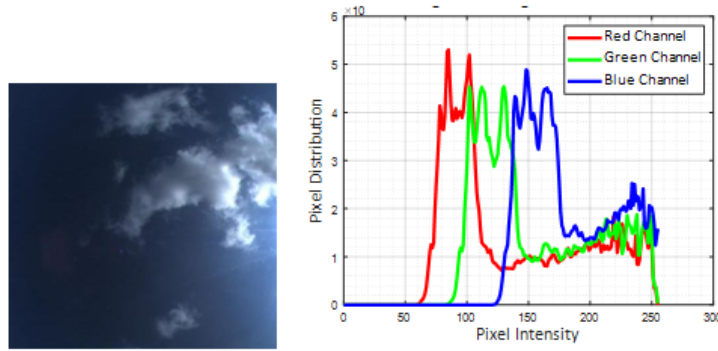


Figure 3: Origin and histogram of Image B

Table 2: Segregation of Image A and B into respective colour channel operations

Red	Green	Blue	Blue - Red	Blue + Red	NBRR

### 3.2. Colour Space Operation for Low-Illumination Sky Images

The histograms of Image C and D are shown in Figure 4 and 5, respectively, where the RGB distribution is extracted from the original photos. Observing

the pixel intensity in the histogram of both images, the green channel is narrow and distinct. It can be inferred that there are no other peaks of distribution  
 110 in the green channel. However, in the red channel, it can be seen that there are multiple peaks with multiple valleys. Most prominently, the blue channel exhibits a noisy distribution at the lower end of the pixel intensity. This is notably true as blue information is deficient in the image. Hence, it is quite clear that the blue channel has little useful information for our analysis.

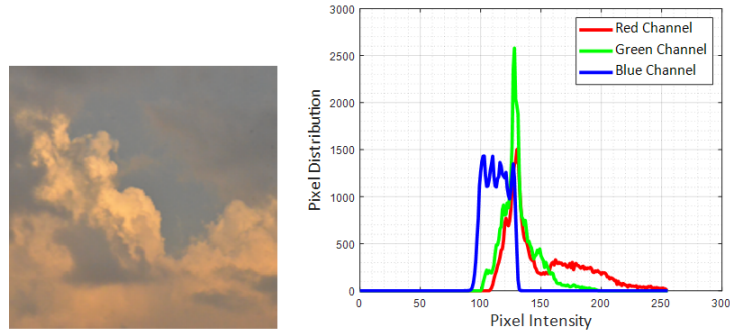


Figure 4: Origin and histogram of Image C

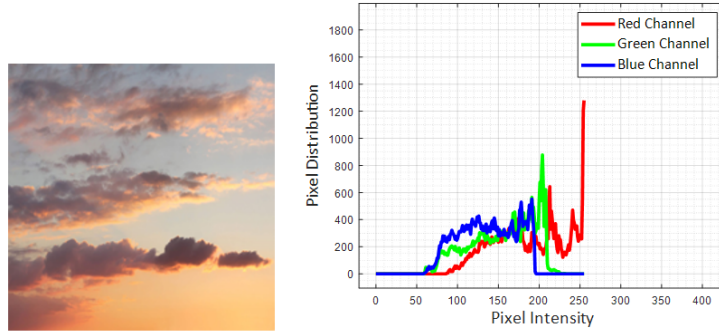


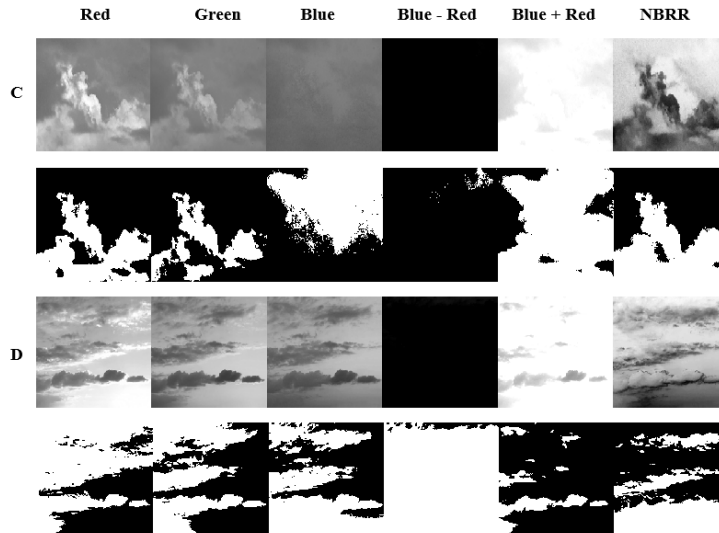
Figure 5: Origin and histogram of Image D

115 Based on the above observation, the histogram RGB spectra shows that the green and red channel contains frequencies that are relatively distinct. The colour spaces are further analyzed by converting the respective RGB colour operations into a binarized image by the Minimum Cross-Entropy Adaptive Thresholding method.

120 Table 3 shows the segmentation of Image C and D using method of colour space operation. As aforementioned, the blue channel results in an erroneous binarized representation of the cloud and sky pixels due to its strident distribution subjacent to the red and green channels. Furthermore, as the presence of blue colour information influences the NBR operation, it is visually evident

125 that the NBRR colour operation manifested signs of error inaccuracy in detecting the clouds. Hence, this justifies that the NBRR colour operation used in the literature of 2011 [3] is not suited for low-illumination conditions.

Table 3: Segregation of Image C and D into respective colour channel operations



The exclusion of blue and NBRR colour operation for low-illumination conditions drives the attention to the analysis of red and green channel. A soaring distribution with other smaller peaks at a particular pixel intensity can be seen in the green channel in the histogram of image C. However, the red channel shows a varying distribution with a distinct valley across the pixel intensities. Examining the segmented images of red and green channels, it is visually clear that numerous areas in the segmented green channel are misclassified as sky pixels. However, the two distinct colours in the red channel provide a better and accurate representation of the cloud and sky components.



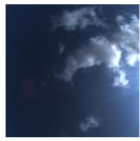
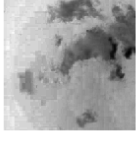




For image D, the opposite conclusion can be drawn. Regions of the red segmented image are mislabeled as sky pixels, whereby the green segmented image presents the true designation of cloud and sky pixels.

### 140 3.3. Proposed Colour Space Operation

In high-illumination cases, there is a clear distinction between the cloud and the sky. However, it is not distinct in low-illumination conditions. There is a difficulty in recognizing the cloud and sky components. Therefore, a different colour channel is proposed. A selection between red or green channel can be employed based on the distribution of the Red and Green channel spectra. This is summarized in Table 4.



Table 4: Recommendation of colour spaces for high and low illumination sky-cloud images

Category	Image	Sky-Cloud Image	Colour Space Image	Channel Operation
<b>High-Illumination</b>	<b>A</b>			Normalised Blue/Red Ratio, NBRR = $\frac{Blue - Red}{Blue + Red}$
	<b>B</b>			
Category	Image	Sky-Cloud Image	Colour Space Image	Channel Operation
<b>Low-Illumination</b>	<b>C</b>			<b>Red (R) Channel</b>
	<b>D</b>			<b>Green (G) Channel</b>

#### 4. Image Segmentation Evaluation

The image segmentation methods adopted for application are Otsu's Fixed Thresholding (FT), Bradley's Adaptive Thresholding (AT), Minimum Cross Entropy (MCE), Adaptive Thresholding (AT), K-Means Clustering (KC) and Simple Linear Iterative Clustering (SLIC), as shown in Figure 6.

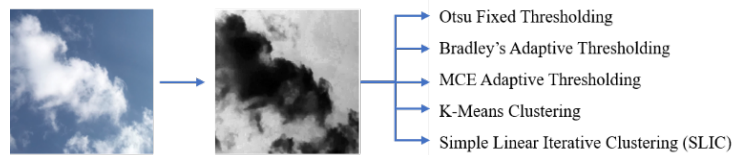


Figure 6: Cloud segmentation process

#### 4.1. Otsu Fixed Thresholding

Global thresholding uses a constant threshold value,  $T$ , to segment the entire image [11]. Otsu’s method of selecting threshold selection from grey-level histogram [12] is adopted to compute the global threshold. This method shows fair results in the division of clear cloud and sky for High-Illumination Image A and Low-Illumination Image D. This is because fixed thresholding favours a good ratio of background to foreground lighting conditions. However, this technique fails when background illumination in the sky varies as depicted in Image B.

#### 4.2. Bradley’s Local Thresholding

Adaptive thresholding considers the spatial variations in illumination of the input cloud image. It computes a different threshold based on the local properties of each pixel and its neighbourhood, thus making it robust to brightness changes. Bradley’s local thresholding uses the linear integral method [13], and this approach exhibits more intuitive results as compared to the fixed thresholding, especially for the low-illumination sky images. This technique does not work well for the high-illumination images because it assumes that the area of interest (foreground) are well distributed in the image. In the situation where the cloud component covers more surface area, the centre of the cloud component will be misclassified as background.

#### 4.3. Minimum Cross-Entropy Local Thresholding

The Minimum Cross-Entropy (MCE) adaptive thresholding is robust and unbiased to histogram [14, 15]. MCE selects a threshold by minimizing the cross-entropy between the original image and the resultant segmented image [6], where useful information is preserved. As a result, MCE demonstrates the most promising result as compared to the rest of segmentation methods.

#### 4.4. K-Means Clustering

K-Means is an unsupervised clustering approach, which groups data based on averages [16]. As this approach is regarded as colour-based segmentation, test results are coherent by visual inspection. However, this approach is prone to issues with the selection for the number of  $k$  initialization clusters, as characteristic of the input cloud images is typically non-uniform. Also, this technique yields misclassification of cloud pixels as sky pixels, notably for thin high-level cirrus clouds.

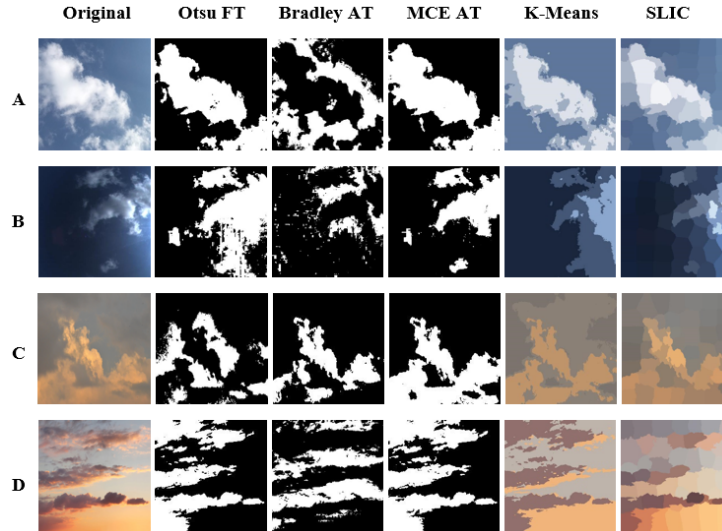
#### 4.5. Simple Linear Iterative Clustering

Superpixel segmentation splits the image into regions, based on texture, contour and continuity similarity [17]. The gradient-based Simple Linear Iterative Clustering Method (SLIC) [18] method is adopted for the evaluation. For ambiguous cloud pixels, similar to K-Means clustering, which comes with a caveat, has tendencies to be mismatched as background pixels.

The comparison of the above image segmentation methods for Image A-D is given in Table 5. The advantages and limitations observed in cloud segmentation

are summarized in Table 6, where the MCE adaptive thresholding has shown to be robust in both high-illumination and low-illumination and selected as the method of choice.

Table 5: Binarization of Image A to D with various segmentation methods



195

## 5. Algorithm

The algorithm proposed in this paper is illustrated in Figure 7. Firstly, based on visual inspection of the image, the input sky-cloud image will be categorized either as high-illumination or low-illumination image. The normalized blue-to-red ratio and a selection of red or green channel is then used to improve the visual contrast for cloud distinction. Subsequently, the images are fed into MCE adaptive thresholding segmentation respectively. After this procedure, the binarized segmented images is used to determine the cloud coverage information. The respective black (0) and white (1) regions will be assigned to sky and cloud components. In the next section, the amount of pixel distribution in each pixel intensity are totalled, for computing the cloud coverage using Cloud Fraction. Lastly, the cloud fraction is verified with the real-time irradiance data for irradiance forecasting.

## 6. Verification of proposed methodology with irradiance data

### 6.1. Cloud Fraction

An evaluation metric for cloud detection called Cloud Fraction [4] measures the percentage of cloud cover in the segmented image. Cloud Fraction (CF) is

Table 6: Advantages and limitations of investigated segmentation methods

<b>Segmentation Method</b>	<b>Advantage</b>	<b>Limitations</b>	<b>Preferred Method</b>
<b>Otsu Fixed Thresholding</b>	Does not need prior image hence, lesser computational complexity	Not suitable for cloud detection uneven brightness in the sky image	
<b>Bradley’s Adaptive Thresholding</b>	Suitable for image with fair cloud distribution	The input must be processed twice, therefore increasing computational cost.	
<b>Minimum Cross-Entropy Adaptive Thresholding</b>	Accurately determine threshold for segmentation while reducing the required computations	May be difficult to identify significantly thin clouds	✓
<b>K-Means Clustering</b>	With a true initialisation of $k$ , the cloud and sky pixels can be classified correctly	Initialisation of $k$ could potentially an issue to achieve cloud pixel accuracy	
<b>Simple Linear Iterative Clustering</b>	Straightforward implement for classification	Does not consider colour information	

defined as the ratio of identified cloud pixels to the overall number of pixels in the image, i.e.,

$$CF = \frac{\text{Cloud Pixels}}{\text{Cloud Pixels} + \text{Sky Pixels}} \times 100\%. \quad (2)$$

215 To obtain CF, the original RGB image is imported into MATLAB, after which  
the red channel was extracted. It is then converted into a 1-bit image using the  
MCE adaptive thresholding, as shown in Figure 8. Null pixels are classified as  
sky pixels and full pixels of value 1 for cloud pixels, as shown in Figure 9. The  
counts of cloud pixels from the histogram are then extracted to calculate the  
220 cloud fraction.

### 6.2. Verification of Cloud Cover with Irradiance Data

The real-time irradiance data and sky images were collected on 11 February, 2018 from 0700 to 1930 to correlate the Cloud Fraction with the irradiance data.

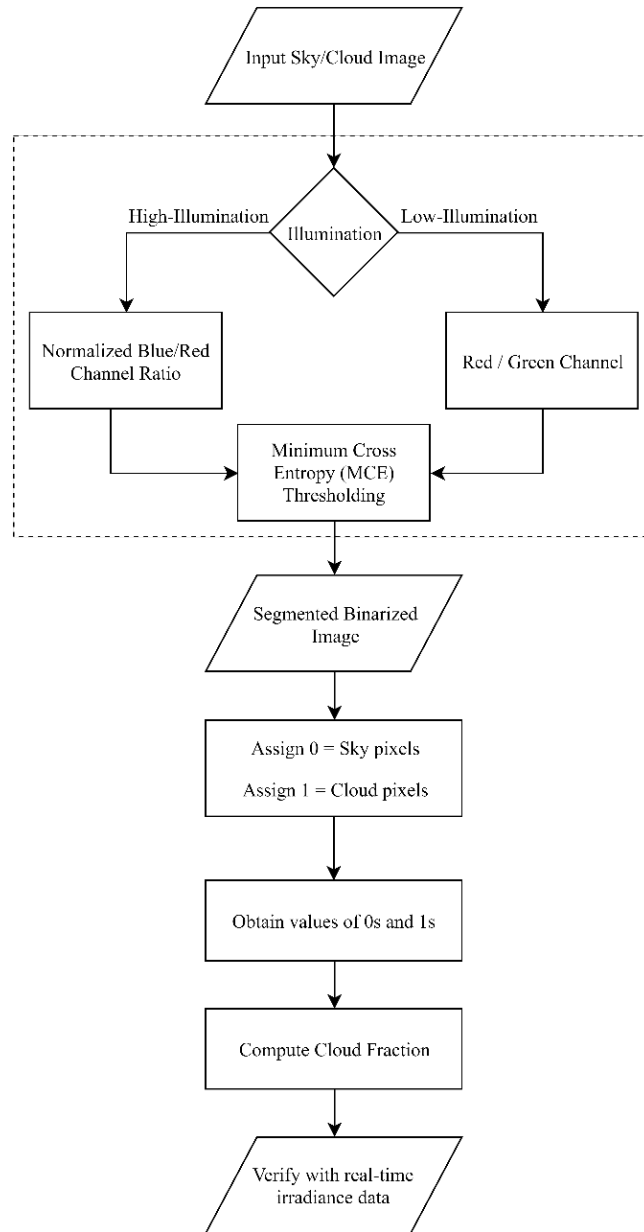


Figure 7: The framework to compute cloud coverage and verification with real-time irradiance data

225 The irradiance data are collected and plotted as a graph, as depicted in Figure 10. With the sky-cloud images captured at the literal timing with the irradiance collection, the cloud fraction is then calculated respectively. A range

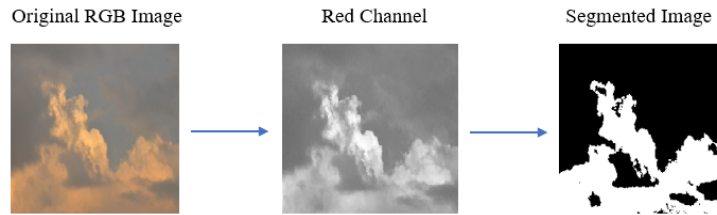


Figure 8: Cloud segmentation process

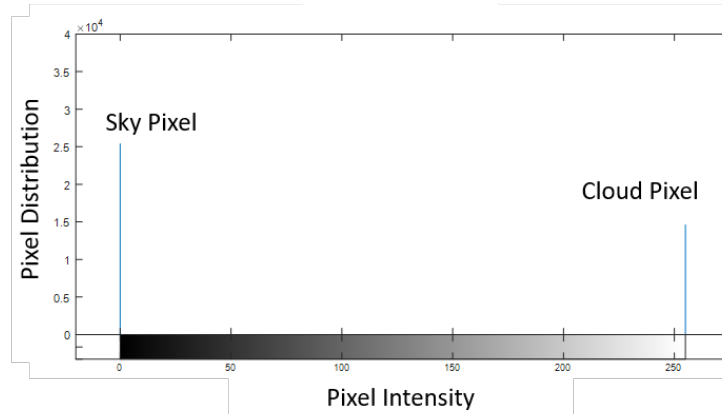


Figure 9: Histogram of binarized segmented image

of irradiance is considered, which covers both the high illumination and low illumination conditions, which were previously discussed in Image A-D that is shown in Figure 6. To improve the effectiveness for analysis, the irradiance graph will be divided into three sections: Before Solar Noon, Solar Noon and After Solar Noon. The dashed green line assumes the smoothed irradiance due to sun path's travel over a day. This is produced by extrapolating between existing irradiance measurements, and removing any abrupt change in irradiance. This information allows the investigation to only focus on the irradiance dips that are observed.

### 6.2.1. Before Solar Noon

The irradiance readings and sky images of 3 points before solar noon are shown in Table 7 and Figure 11, respectively. At point A, zero cloud fraction is observed as there no clouds are present. However, at Point B, with a cloud fraction of 3.9%, the irradiance reduces by  $82.6 \text{ W/m}^2$ . As the cloud fraction progresses back to 0%, an increase of irradiance value was observed.

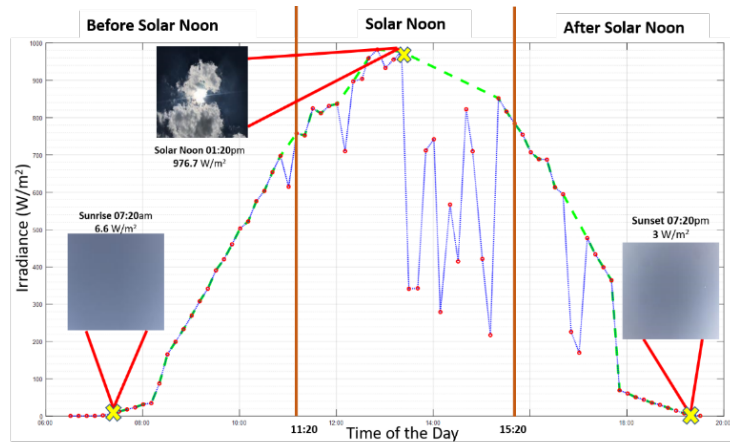


Figure 10: Measured Irradiance

Table 7: Irradiance & Cloud Fraction before Solar Noon

Point	Time (Hrs)	Irradiance ( $W/m^2$ )	Cloud Fraction (%)
A <sub>1</sub>	1050	697.6	0
B <sub>1</sub>	1100	615	3.9
C <sub>1</sub>	1110	757.8	0

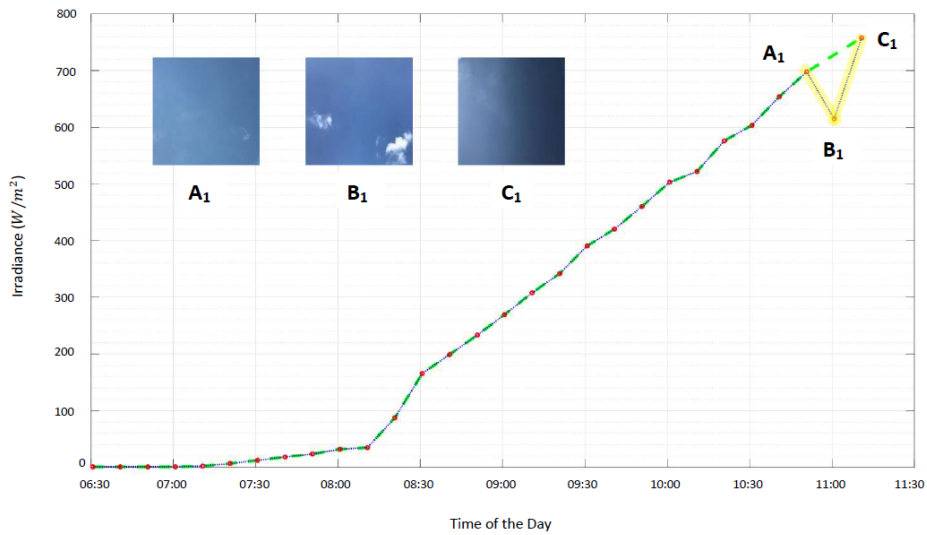


Figure 11: Irradiance Graph before Solar Noon

### 6.2.2. During Solar Noon

The irradiance readings and sky images of 19 points during solar noon are shown in Table 8 and Figure 12, respectively. An identical trend can be drawn that relates the cloud cover and irradiance data. An apparent section involving the solar noon at point G to point J (30 minutes after solar noon) will be further extracted for analysis.

Table 8: Irradiance & Cloud Fraction during Solar Noon

Point	Time (Hrs)	Irradiance (W/m <sup>2</sup> )	CF (%)	Point	Time (Hrs)	Irradiance (W/m <sup>2</sup> )	CF (%)
A <sub>2</sub>	1200	837	0	K <sub>2</sub>	1400	742.1	25.3
B <sub>2</sub>	1210	710	42.2	L <sub>2</sub>	1410	279.1	72.7
C <sub>2</sub>	1220	897	29.8	M <sub>2</sub>	1420	567	63.8
D <sub>2</sub>	1250	982.5	30.1	N <sub>2</sub>	1430	414.6	82.8
E <sub>2</sub>	1300	933.3	29.6	O <sub>2</sub>	1440	822.4	41.3
F <sub>2</sub>	1310	955.4	0	P <sub>2</sub>	1450	709.9	48.4
G <sub>2</sub>	1320	976.7	39.2	Q <sub>2</sub>	1500	421.4	53.7
H <sub>2</sub>	1330	341.4	79.3	R <sub>2</sub>	1510	217.2	68.3
I <sub>2</sub>	1340	342.6	82.4	S <sub>2</sub>	1520	851.9	7.71
J <sub>2</sub>	1350	712	67.7				

As shown in Figure 13, at initial Point G, 39.2% of the image is calculated as cloud fraction. 10 minutes after solar noon, an increase of cloud cover to 79.3% reduces the irradiance immensely by 65%. At point J, the cloud fraction decreases to 67.7% that leads to an increase in irradiance. It can be inferred that the presence of cloud cover affects the irradiance drop drastically.

### 6.2.3. After Solar Noon

The irradiance readings and sky images of 4 points after solar noon are shown in Table 9 and Figure 14, respectively. Akin to the previous sections, a similar conclusion can be deduced that cloud cover heavily influences the irradiance received on the PV panel and irradiance sensor.

A statistical metric named Pearson Correlation Coefficient is calculated to evaluate the association between cloud fraction and irradiance data. The coefficient index,  $r$ , determines the strength and the relationship between the variables. However, only data where cloud fraction affects the irradiance are considered for the correlation calculation. Table 10 shows the respective  $x$  (cloud fraction) and  $y$  (irradiance difference) values. The correlation coefficient,  $r$ , is



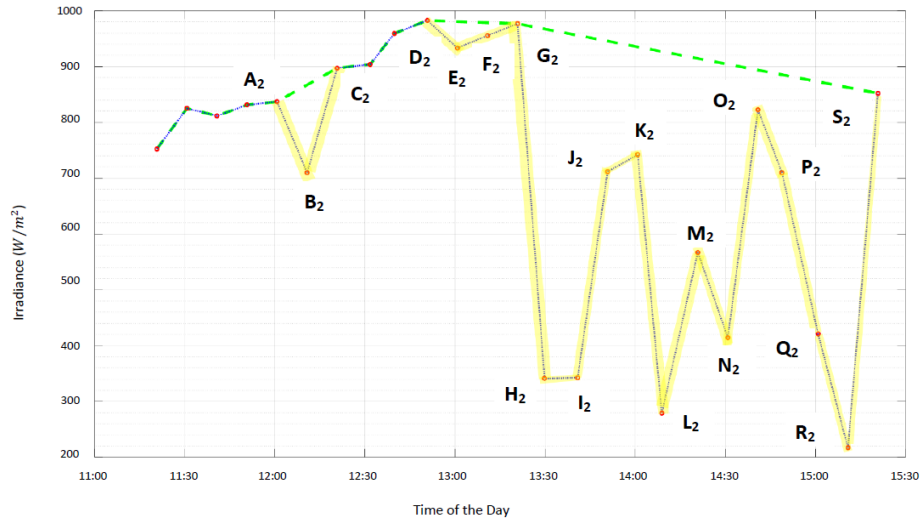


Figure 12: Irradiance Graph during Solar Noon

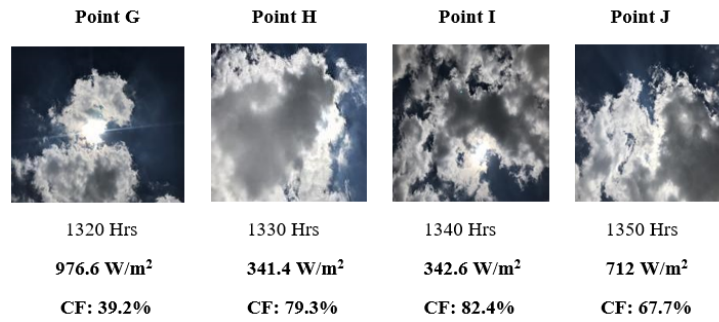


Figure 13: Irradiance and sky-image of Point G-J

Table 9: Irradiance & Cloud Fraction after Solar Noon

Point	Time (Hrs)	Irradiance (W/m <sup>2</sup> )	CF (%)
A <sub>3</sub>	1640	594.7	10.2
B <sub>3</sub>	1650	226	28.5
C <sub>3</sub>	1700	170	26
D <sub>3</sub>	1710	477.2	13

yield by

$$r = \frac{n \sum xy - \sum x \sum y}{\sqrt{[x \sum x^2 - (\sum x)^2][n \sum y^2 - (\sum y)^2]}} = 0.668.$$

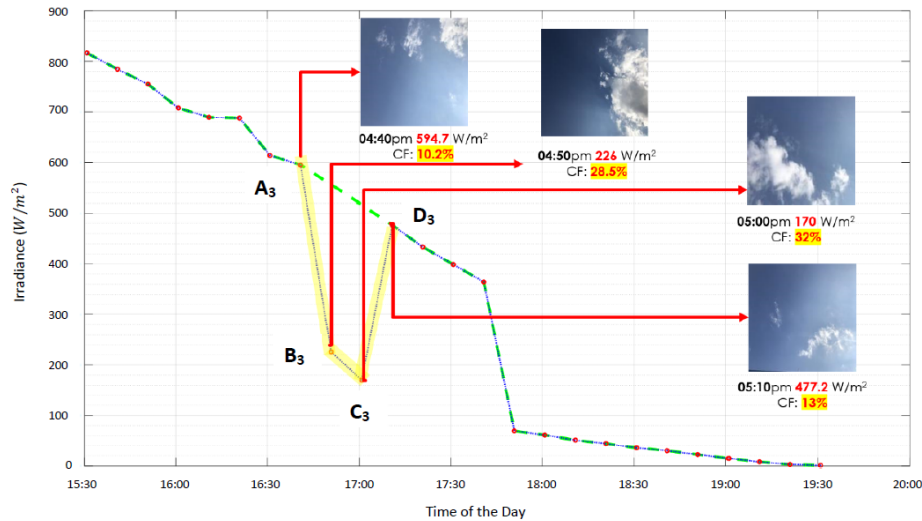


Figure 14: Irradiance Graph after Solar Noon

265 This shows a positive linear relationship between cloud fraction and irradiance  
 data.

### 6.3. Limitations

270 Despite the consistent trend, certain limitations were observed, as shown in  
 Table 11. Data in the table shows hikes in the irradiance with the increment of  
 cloud fraction. This observation provides a contrasting difference as compared to  
 the concluded trend. There could be numerous feasible reasonings why this  
 may occur.

- 275 1. At present, the geographical area of sky-cloud image acquisition is sur-  
 rounded by neighboring buildings from all sides. The heavily affects the  
 downward light that lands on the irradiance sensor.
2. The slight deviation in the extremely low irradiance measurements after  
 solar noon does not provide any change in computed cloud fraction. How-  
 ever, this is not a useful case for irradiance forecasting. Such durations of  
 low irradiance may occur, depending on day to day meteorological condi-  
 280 tions.
3. As the images are taken parallel to the panel, adjacent to the pyranometer,  
 a portion of the sky that is directly above the pyranometer is captured.  
 In this setup, it is observed that the presence of cloud cover on these  
 images has correlated with abrupt drops in irradiance in our study before  
 285 and after solar noon. However, the correlation might be stronger if a  
 wide-angle or fish-eye lens are used in this study.
4. The irradiance sensor has an error reading deviation of +10% to +15%.

Table 10: Pearson Correlation Coefficient Tabulation

Category	n	x (Cloud Fraction, %)	y (Irradiance Difference, W/m <sup>2</sup> )	xy	x <sup>2</sup>	y <sup>2</sup>
<b>Before Solar Noon</b>	1	3.9	82.6	322.1	15.2	6,822.8
<b>During Solar Noon</b>	2	42.2	127	5,359.4	1,780.8	16,129
	3	0.5	19.2	9.6	0.25	368.6
	4	40.1	635.3	25,475.5	1,608.01	403,606.1
	5	47.4	463	21,946.2	2,246.8	214,369
	6	19	152.4	2,895.6	361	23,225.8
	7	7.1	112.5	798.8	50.4	12,656.3
	8	5.3	288.5	1,529.1	28.1	83,232.3
	9	14.6	204.2	2,981.3	213.2	41,697.6
<b>After Solar Noon</b>	10	18.3	368.7	6,747.2	334.90	135,939.7
	11	3.5	56	196	12.3	3,136
		$\sum x = 201.9$	$\sum y = 2539.4$	$\sum xy =$ 68,275.8	$\sum x^2 =$ 6,650.87	$\sum y^2 =$ 943,235.08
		$(\sum x)^2 =$ 40,73.61	$(\sum y)^2 =$ 6,448,552.36			

Table 11: Pearson Correlation Coefficient Tabulation

<b>Before Solar Noon</b>			<b>Solar Noon</b>			<b>After Solar Noon</b>		
Time	Irradiance (W/m <sup>2</sup> )	CF (%)	Time	Irradiance (W/m <sup>2</sup> )	CF (%)	Time	Irradiance (W/m <sup>2</sup> )	CF (%)
<b>0920</b>	341.7	0	<b>1140</b>	811.6	30.6	<b>1840</b>	30.3	0
<b>0930</b>	390.7	28.5	<b>1150</b>	831.1	37.6	<b>1850</b>	22.6	0
<b>0940</b>	420.3	5.4	<b>1200</b>	837	0	<b>1900</b>	14.8	0

Nevertheless, these factors do not affect the investigation eminently, as verified with the pyranometer.

## 290 7. Conclusion

The RGB colour model was adopted to work with cloud detection. As such, a recommendation of colour channel operations is proposed. Primarily, the NBRR operation for the high-illumination condition, and a selection of a red or green channel for the low-illumination condition. A literature review of existing state-of-the-art has been performed. Experimental evaluation shows that MCE adaptive thresholding has demonstrated the highest potential for accurate cloud segmentation under both high and low illumination condition. The metric for measuring the amount of cloud coverage in a sky-cloud image shows a strong relationship with the irradiance data. It has been demonstrated that an increment of Cloud Fraction reduces the irradiance value. Also, a linear positive correlation coefficient of +0.67 was observed between Cloud Fraction and real-time irradiance data.

## References

- [1] M. Bieri, K. Winter, S. Tay, A. Chua, T. Reindl, An irradiance-neutral view on the competitiveness of life-cycle cost of pv rooftop systems across cities, *Energy Procedia* 130 (2017) 122–129. doi:10.1016/j.egypro.2017.09.408.
- [2] S. Song, K. Poh, Solar PV leasing in Singapore: Enhancing return on investments with options, *IOP Conference Series: Earth and Environmental Science* 67 (2017) 12–20. doi:10.1088/1755-1315/67/1/012020.
- [3] D. Yang, Z. Ye, L. Lim, Z. Dong, Very short term irradiance forecasting using the lasso, *Solar Energy* 114 (2015) 314–326. doi:10.1016/j.solener.2015.01.016.
- [4] M. Souza-Echer, E. Pereira, L. Bins, M. Andrade, A simple method for the assessment of the cloud cover state in high-latitude regions by a ground-based digital camera, *Journal of Atmospheric and Oceanic Technology* 23 (3) (2006) 437–447. doi:10.1175/jtech1833.1.
- [5] Z. Peng, D. Yu, D. Huang, J. Heiser, S. Yoo, P. Kalb, 3D cloud detection and tracking system for solar forecast using multiple sky imagers, *Solar Energy* 118 (2015) 496–519. doi:10.1016/j.solener.2015.05.037.
- [6] Q. Li, W. Lu, J. Yang, A hybrid thresholding algorithm for cloud detection on ground-based color images, *Journal of Atmospheric and Oceanic Technology* 28 (10) (2011) 1286–1296. doi:10.1175/jtech-d-11-00009.1.
- [7] S. Liu, L. Zhang, Z. Zhang, C. Wang, B. Xiao, Automatic cloud detection for all-sky images using superpixel segmentation, *IEEE Geoscience and Remote Sensing Letters* 12 (2) (2015) 354–358. doi:10.1109/lgrs.2014.2341291.

- 330 [8] R. Chauvin, J. Nou, S. Thil, A. Traoré, S. Grieu, Cloud detection methodology based on a sky-imaging system, *Energy Procedia* 69 (2015) 1970–1980. doi:10.1016/j.egypro.2015.03.198.
- [9] J. Yang, W. Lu, Y. Ma, W. Yao, An automated cirrus cloud detection method for a ground-based cloud image, *Journal of Atmospheric and Oceanic Technology* 29 (4) (2012) 527–537. doi:10.1175/jtech-d-11-00002.1.
- 335 [10] S. Dev, Y. Lee, S. Winkler, Color-based segmentation of sky/cloud images from ground-based cameras, *IEEE Journal of Selected Topics in Applied Earth Observations and Remote Sensing* 10 (1) (2017) 231–242. doi:10.1109/jstars.2016.2558474.
- 340 [11] M. Sonawane, C. Dhawale, A brief survey on image segmentation methods, *IJCA Proceedings on National conference on Digital Image and Signal Processing DISP 1* (2015) 1–5.
- [12] N. Otsu, A threshold selection method from gray-level histograms, *IEEE Transactions on Systems, Man and Cybernetics* 9 (1979) 62–66. doi:10.1109/TSMC.1979.4310076.
- 345 [13] D. Bradley, G. Roth, Adaptive thresholding using the integral, *Image Journal of Graphics Tools* 12 (2007) 13–21. doi:10.1080/2151237X.2007.10129236.
- [14] C. Li, C. Lee, Minimum cross entropy thresholding, *Pattern Recognition* 26 (4) (1993) 617–625. doi:10.1016/0031-3203(93)90115-d.
- 350 [15] C. Li, P. Tam, An iterative algorithm for minimum cross entropy thresholding, *Pattern Recognition Letters* 19 (8) (1998) 771–776. doi:10.1016/S0167-8655(98)00057-9.
- 355 [16] D. Nameirakpam, K. Manglem, Y. Jina Chanu, Image segmentation using k-means clustering algorithm and subtractive clustering algorithm, *Procedia Computer Science* 54 (2015) 764–771. doi:10.1016/j.procs.2015.06.090.
- [17] Ren, Malik, Learning a classification model for segmentation, *Proceedings Ninth IEEE International Conference on Computer Vision* 1 (2003) 10–17. doi:10.1109/ICCV.2003.1238308.
- 360 [18] R. Achanta, A. Shaji, K. Smith, A. Lucchi, P. Fua, S. Susstrunk, Slic superpixels compared to state-of-the-art superpixel methods, *IEEE Transactions on Pattern Analysis and Machine Intelligence* 34 (11) (2012) 2274–2282. doi:10.1109/TPAMI.2012.120.